Bidirectional, Thin-Film Repulsive-/Attractive-Force Electrostatic Actuators for a Crawling Milli-Robot

Ethan W. Schaler,[1] Loren Jiang,[2] Caitlyn Lee,[3] and Ronald S. Fearing[1,*]

***Abstract*— We demonstrate a new thin-film electrostatic actuator (RAFA) capable of generating bidirectional repulsive- and attractive-forces. The two-layer actuator controllably produces measured electrostatic pressures up to 156 Pa (38.9 mN, for 2.5 cm^2 electrode area) in repulsion and 352 Pa (88.0 mN) in attraction when operating at 0–1.2 kV. The four patterned electrodes (two per layer) have a cross-section geometry optimized in simulation for maximum blocked force over a 25–500 μm stroke length. RAFAR, a 132 mg milli-robot, uses a 1.45 cm^2 RAFA to crawl at 0.32 mm/s with anisotropic friction feet.**

I. Introduction

An array of novel μm- to cm-scale actuation technologies have enabled the proliferation of mobile meso-scale robots in recent years.

Numerous mm- to cm-scale robots employ electrostatic actuators: a multi-phase electrostatic film motor with electroadhesion [1], [2], an oscillating electrostatic film actuator inducing robot body vibrations [3], paper zipper actuators with anisotropic friction feet [4], and scratch drive actuators providing inchworm locomotion [5], [6]. All use attractive-force electrostatic actuators, and all except [3], [5] use tethered operation. Electrostatic actuators operate with few moving parts, simple control signals, and forces proportional to applied voltages.

Other meso-scale robots are powered by piezoelectric actuators – flying insect [7], myriapod [8], HAMR-V/F [9], [10], LPMR [11] – by shape memory alloy actuators – RoACH [12], MEDIC [13], HAMR [14] – and by magnetic actuators [15], [16]. Finally, vibration-induced ambulation of robots has been achieved in a silicon hexapod [17] (via substrate excitation), Resbot [18] (using electromagnetic motors), and the previously mentioned electrostatic- [3] and piezoelectric- [11] actuator powered robots.

In this paper, we present a new bidirectional, thin-film Repulsive-/Attractive-Force electrostatic Actuator (RAFA), and use it to construct a 132 mg milli-robot (Fig. 1). RAFAs generate active, voltage-controlled forces throughout the full actuation cycle (both extension and retraction), yielding larger work-loops than unidirectional actuators with passive spring returns (Fig. 6) [3], [4], [6]. RAFAs use simple integrated springs and spacers for alignment (bidirectional slider film motors need tensioners, yaw guards, etc. [2]), and employ no exotic materials or manufacturing processes.

[1] E. Schaler and R. Fearing are with the Dept. of Electrical Engineering and Computer Science, University of California (Berkeley), USA.

[2] L. Jiang is with the Dept. of Bioengineering, University of California (Berkeley), USA.

[3] C. Lee is with the Dept. of Mechanical Engineering, El Camino College, USA.

[*] Correspondence: R. Fearing (*ronf@berkeley.edu*)

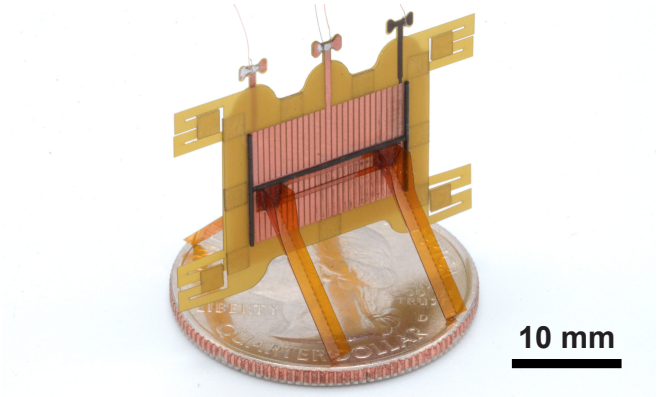

Fig. 1: RAFAR, a 132 mg thin-film crawling milli-robot with integrated repulsive-/attractive-force electrostatic actuator.

II. Background

Electrostatic actuators consist of sets of differentially-polarized electrodes that operate in one of two modes: attractive-force actuators (AFAs) generate attractive forces and gap-closing motion while repulsive-force actuators (RFAs) generate repulsive forces and gap-opening motion [19]. AFAs have unstable operation (pull-in instability) and stroke length is limited by the initial electrode gap. RFAs have open-loop stable operation (force, displacement are directly proportional to voltage) and stroke length is limited only by the electric field strength [19]. Both RFAs and AFAs can operate in series to increase stroke length [20]–[23].

RFAs were initially developed by Tang, *et al.* [24], to levitate the moving electrodes in a MEMS resonator. He, *et al.* further investigated MEMS RFA designs [25], simulated multi-level actuators [26], and fabricated 1- and 2-DoF micro-mirrors [27], [28] and low-voltage actuators [29].

Schaler, *et al.* [19] introduced cm-scale linear and rotational thin-film RFAs with a new, higher-force electrode pattern. Then, [20] demonstrated multi-layer thin-film RFAs and a 2-DoF micro-mirror. Thin-film RFAs consist of metal foil / polyimide composites that are inexpensive, simple to fabricate, and allow greater flexibility in electrode configurations or multi-layer devices than MEMS equivalents.

RAFAs employ 2 control signals to selectively operate 1 actuator as a RFA or AFA, and achieve bidirectional actuation. Bidirectional motion with 2 antagonistic actuators was shown using AFAs [30], RFAs [20], and bimorph piezoelectric actuators [31]. Bidirectional motion of 1 MEMS electrode operated as a RFA / AFA was shown in [32], but required individual control signals to 6+ adjacent electrodes.

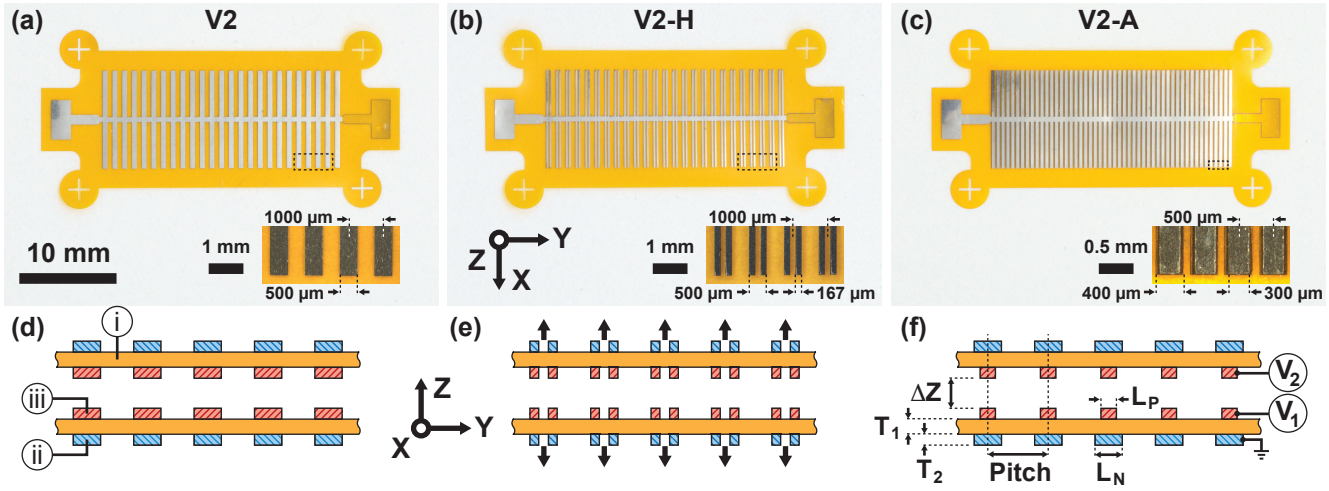

Fig. 2: Flexible, two-layer repulsive force actuator designs fabricated in this work: (a) V2, the electrode design used in E. Schaler, et al. [19], (b) V2-H, an improved design with hierarchical electrodes, (c) V2-A, an improved design with asymmetrical electrodes. For each actuator electrode design, the two functional layers are photographed (a-c) and the cross-sections are illustrated (d-f). Each actuator layer is composed of a polyimide substrate (i) with negative (ii) and positive (iii) electrodes. Actuator layers experience a net repulsive electrostatic pressure, illustrated in (e). Actuator dimensions include the substrate ($T_1 = 60\ \mu m$) and electrode ($T_2 = 12.5\ \mu m$) thickness, positive (L_P) and negative (L_N) electrode width, pitch ($Pitch$), and inter-layer height (ΔZ), listed hereafter as $\underline{x}$ = [L_P, L_N, $Pitch$]. For V2, $\underline{x}$ = [500, 500, 1000] μm ($L_P = L_N = Pitch/2$); for V2-H, $\underline{x}$ = [167, 167, 1000] μm in clusters of two electrodes separated by 333 μm pitch; for V2-A, $\underline{x}$ = [300, 400, 500] μm.

III. Simulation

Three actuator electrode designs are investigated for maximizing repulsive-work (see Fig. 2):

- **V2** Symmetric electrodes, all of equivalent size / pitch
- **V2-H** Hierarchical electrodes, all of equivalent size but clustered in groups by varying pitch
- **V2-A** Asymmetrical electrodes, with consistent pitch but positive / negative electrodes of non-equivalent size

(**V1** and **V2** electrode designs are compared in [19])

In each case, the actuator layers are modeled with dimensions equivalent to the fabricated actuator layers in Sec. IV-A. Positive and negative metal electrodes are defined on opposing sides of an insulating substrate (a continuous dielectric film) and offset by a patterned adhesive film.

For each RFA design, the electric potential (V), electric field ($\underline{E}$) vector, and corresponding bound / free surface (σ_b, σ_f) and volumetric (ρ_b, ρ_f) charge densities are calculated via finite differences simulation. Details on numerical simulation of RFAs can be found in E. Schaler, *et al.* [19] and alternate models are presented in [25]–[27]. The electrostatic force on a region of the actuator is:

$$\underline{F} = \iiint_{\mathbb{V}_E} (\rho_f \underline{E}) d\mathbb{V} + \iiint_{\mathbb{V}_D} (\rho_b \underline{E}) d\mathbb{V} + \iint_{\mathbb{S}} (\frac{1}{2}(\sigma_f + \sigma_b)\underline{E} \cdot \hat{n}) d\mathbb{S} \quad (1)$$

with force contributions from the electrode ($\mathbb{V}_E$) and dielectric ($\mathbb{V}_D$) volume interiors and the interfacing surfaces between these regions ($\mathbb{S}$, with surface normal vector $\hat{n}$). The electrostatic pressure is calculated by dividing the electrostatic force by electrode area. The actuator work (W):

$$W = \int_{\Delta Z_0}^{\Delta Z_1} \underline{F}(\Delta Z) dZ \quad (2)$$

is estimated by piecewise integration of the electrostatic force at a range inter-layer heights (ΔZ). Subsequently the V2-A design was also modeled with the RAFA electrode polarization to determine attractive force and work over an equivalent range.

A. Optimization

The work-optimized electrode geometry is determined by solving the nonlinear, convex optimization problem:

$$\min_{\underline{x}} -W(\underline{x}), \text{ with } \underline{x} = [L_P, L_N, Pitch] \quad (3)$$

$$W(\underline{x}) = P(\underline{x}) \cdot \int_{\Delta Z_0}^{\Delta Z_1} F_z(\underline{x}, \Delta Z) dZ \quad (4)$$

$$P(\underline{x}) = \frac{F_z(\underline{x}, \Delta Z, \Delta Y)}{F_z(\underline{x}, \Delta Z, 0)} \quad (5)$$

subject to constraints:

$$\begin{aligned} & L_P, L_N \in [250\mu m, 1000\mu m] \\ & Pitch \geq L_P, L_N \\ & Pitch \leq 5000\mu m \end{aligned} \quad (6)$$

Work (W) is maximized for a given actuator electrode geometry ($\underline{x}$) (3), and calculated by piecewise integration of the normal component of the actuator force (F_z) at a range inter-layer heights $\Delta Z \in [\Delta Z_0, \Delta Z_1] = [25, 500]\ \mu m$

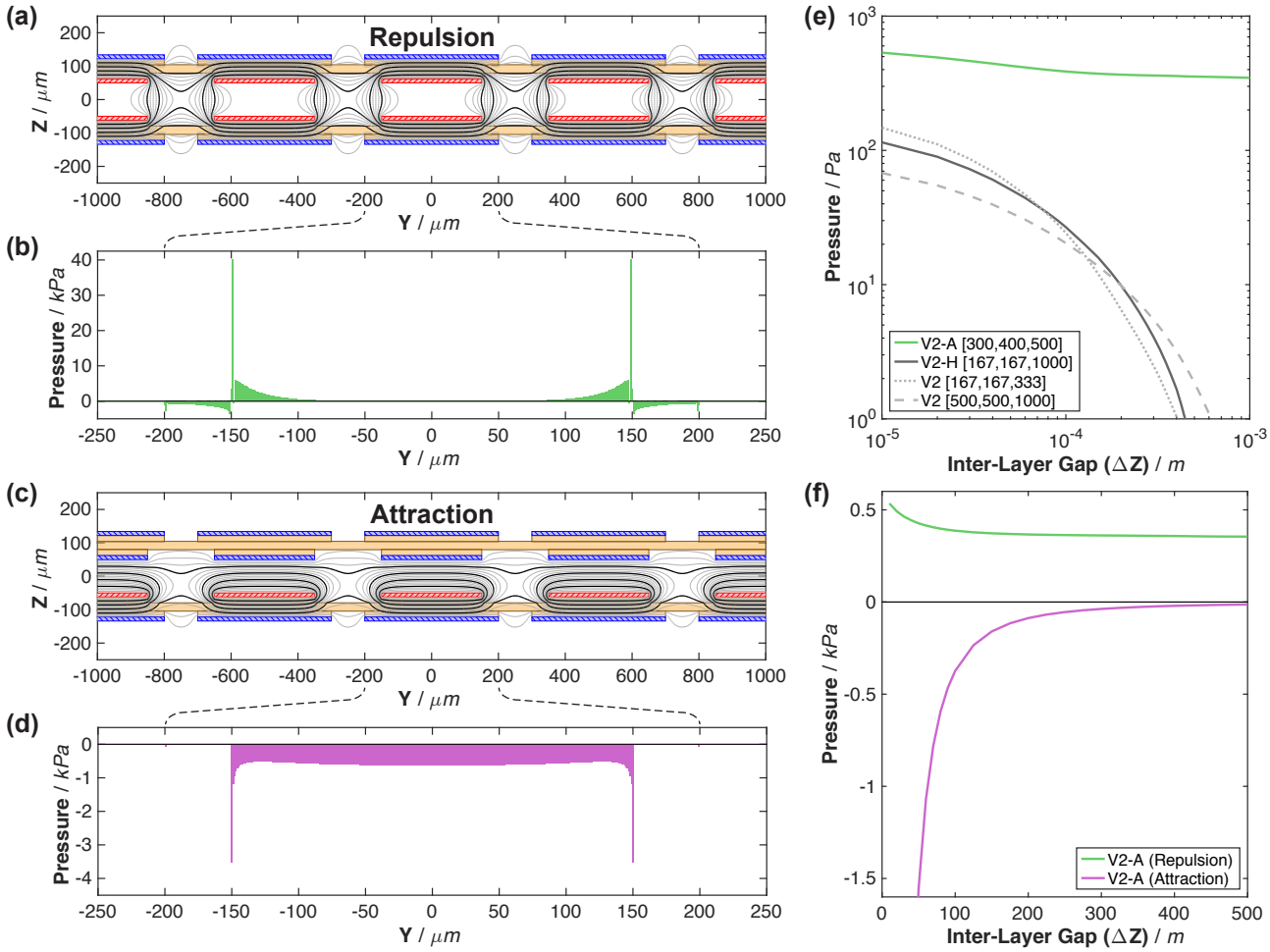

Fig. 3: Simulation results for the bidirectional repulsive- / attractive-force electrostatic actuator. (a/c) Electrostatic potential (V) for V2-A design, with electrodes operating at 0 kV (blue) / 1.2 kV (red) and dielectric substrate (orange). (b/d) Net electrostatic pressure across the top layer of the V2-A design, focusing on the center electrode and with 1 μm mesh size. (a-b) are operating in repulsion-mode; (c-d) are operating in attraction-mode. (e) Net electrostatic pressure produced by a complete actuator versus layer separation (ΔZ) in each design, with dimensions of $\underline{x}$ = [L_P,L_N,$Pitch$]. Operating voltage is 1.2 kV. (f) Net electrostatic pressure produced by a complete V2-A actuator versus layer separation (ΔZ) in both repulsion- and attraction-modes.

(4). A misalignment penalty (P) is imposed on the work calculation to prevent the optimization from converging to a solution with alignment requirements beyond manufacturing capabilities (5). Here, a misalignment of $\Delta Y = 25\ \mu m$ is used and the force decrease is compared at $\Delta Z_0 = 25\ \mu m$.

Constraints (6) are imposed by physical limitations on minimum feature size (100 μm) for fabrication / alignment, on minimum pitch (greater than electrode widths), and on maximum feature size (1000 μm) for a reasonably compact actuator system and to limit the search space.

The optimization problem is solved in Matlab using the $fmincon$ nonlinear programming solver and sequential quadratic programming (SQP) algorithm.

B. Repulsive-Force Operation

The V2,V2-H, and V2-A RFA electrode designs are compared in Fig. 3.

The V2 symmetric electrode design (Fig. 2a/d), first presented in [19], employed equal-sized positive and negative electrodes $\underline{x}$ = [500, 500, 1000] μm, which provided a decent balance of high peak force (increases with smaller unit cells), and force reduction at greater ΔZ offsets (decreases as inter-layer distance increases, and decreases faster with smaller unit cells). This behavior is evident when comparing $\underline{x}$ = [500, 500, 1000] μm and $\underline{x}$ = [167, 167, 333] μm in Fig. 3e.

The V2-H hierarchical electrode design (Fig. 2b/e) provides a compromise on the performance of both large and small unit cell sizes in the V2 design. For this V2-H [167, 167, 1000] μm pattern, peak force is higher than the V2 [500, 500, 1000] pattern at all $\Delta Z \leq 200\ \mu m$ (due to a greater number of fringing fields) and higher than the V2 [167, 167, 333] unit cell design at distances of $\Delta Z > 70\ \mu m$ (due to a more gradual reduction in force at larger ΔZ).

The V2-A asymmetric electrode designs (Fig. 2c/f) are

quite different: positive and negative electrodes are of unequal size, and pitch is less than twice the electrode widths (to reduce unit cell size and increase electrode density). This V2-A electrode design was discovered during the course of the parameter space exploration for the work-optimization simulations. The V2-A design with $\underline{x}$ = [300, 400, 500] μm used in the majority of this paper was derived from the optimal design $\underline{x}$ = [307, 391, 451] for a ΔY = 10 μm misalignment penalty. L_P, L_N parameters were rounded to the nearest 100 μm, and $Pitch$ was increased to L_N + 100 μm to conform to manufacturing tolerances. An interesting simulation result of these designs is the force reduction trend as ΔZ increases: the typical $F \propto \Delta Z^{-2}$ fall-off in force is less pronounced at $\Delta Z \geq 150$ μm and sustained 0.35–0.36 kPa pressures are predicted even at $\Delta Z \geq 500$ μm gaps. Note that this behavior is not reflected in the measured actuators (Fig. 6).

C. Bidirectional Repulsive-/Attractive-Force Operation

A new capability of these V2 / V2-H / V2-A electrode geometries is the ability to generate both repulsive- and attractive-forces (Fig. 3a-d/f). This requires the use of two channels to independently control the potential on each actuator layer: layers generate a *net repulsive force* when the two internal electrodes operate at V_+; layers generate a *net attractive force* when the two internal electrodes differentially operate at $V_1 \ll V_2$ (or vice versa).

As seen in Fig. 3f, both repulsive- and attractive-forces scale inversely proportional to displacement. Electrostatic pressures of 0.43–0.36 kPa (repulsion) and -1.55– -0.055 kPa (attraction) are generated with the same V2-A electrode geometry and ΔZ = 25–250 μm range of inter-layer gaps.

IV. Actuator Development

The V2-A electrode design was selected to be fabricated (Fig. 2) and characterized (Fig. 4–6).

A. Fabrication

RFA layers are fabricated using both an in-house laser-cutting process (introduced in [20] for rapid iterative design) and a commercial wet-etching process at a flex-PCB manufacturer (replaced an in-house wet-etching process [19]).

In the laser-cutting process (see [20]): layers are composed of stainless steel electrodes (Trinity Brand Industries, 12.7 μm) on a polyimide substrate (DuPont, Kapton FPC, 25 μm), bonded together with thermally-activated sheet adhesive (GBC, Octavia Hot Mount Adhesive, 17.5 μm).

The electrodes are prepared by cleaning a sheet of stainless steel, laminating thermal adhesive to one side, and securing the other side to GelPak (with the adhesive face-up). The substrate is prepared by cleaning the Kapton and securing it to another GelPak surface. The actuator electrode pattern and substrate extents are cut into the respective material layers using a UV laser cutter (PhotoMachining Inc., 355 nm laser). Excess mask and substrate material are removed manually. The substrate / electrode layers are run through a laminator to set the thermal adhesive. Any exposed thermal adhesive is removed with acetone (Fischer Scientific). Production time is approximately 2–3 hours per sheet of actuator layers (compared to >4 hours for the wet-etching process in [19]).

In the wet-etching process (see [19]): layers are composed of a flexible circuit composite (Dupont, Pyralux AP8515) with 18 μm copper foil electrodes bonded to each side of a 25 μm polyimide substrate.

A commercial manufacturer of flexible circuit boards (The Boardworks) was used to pattern an array of two-sided actuator layers (72 layers at $3.40 per layer) on a single 9 x 12 $inch$ sheet of Pyralux AP. The copper foil was etched in a wet-etch process, with electrode patterns aligned on both sides of the polyimide substrate. The polyimide substrate was subsequently patterned using the UV laser cutter. The resulting individual actuator layers (cut out of the full sheet) contain patterned electrodes surrounded by 4 polyimide suspension springs.

RAFA layers can optionally adhere film spacers (50–100 μm thick) or an extra polyimide film insulator (25 μm) over the V_+ electrode on one layer for shorting protection between layers during attractive-mode operation.

B. Process Trade-offs

As introduced above, there are three processes currently available for RFA / RAFA fabrication: in-house laser-cutting or wet-etching processes, and out-sourced commercial wet-etching. The processes are compared in Table I.

The in-house processes are ideal for iterative prototyping of new robots, actuators, or electrode patterns, but produce lower electrostatic pressures due to worse electrode alignment / accuracy or thicker substrates. The commercial flexible circuit fabrication process allows anyone to produce large quantities of actuators with higher pressures, consistently accurate electrode patterns, and the best electrode alignment.

Future fabrication process iterations could also employ a conductive ink printing processes for roll-to-roll bulk fabrication on thin-film substrates.

C. Characterization

The repulsive forces of the fabricated actuator layers were characterized using the same blocked-force testing apparatus presented in [19]. The actuator layers are laminated to glass slides. The first layer is secured to an XY-stage; the second layer is mounted to the load cell and Z-stage with a wax interface (for proper leveling). Actuators are controlled by a DAQ (NI, USB-6341) and Labview, and powered by high-voltage amplifiers (Trek, PZD700 / XP Power, G-60).

Table I: Comparison of actuator fabrication processes.

Metric	Laser (IH)	Etch (IH)	Etch (C)
Prototype Fabrication	+	o	–
Bulk Fabrication	o	–	+
Electrostatic Pressure	–	o	+
Electrode Dimensional Accuracy	+	–	o
Electrode Alignment (2-Sided)	o	–	+

(IH) – In-House **(C)** – Commercial

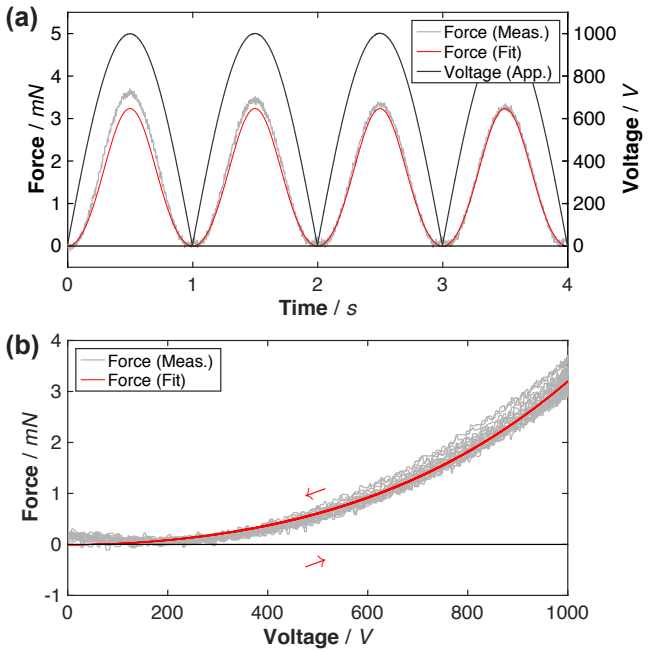

Fig. 4: RFA with V2-A electrode pattern generating repulsive-forces at ΔZ = 100 μm and 0–1.0 kV. (a) Applied square-root of sinusoid voltage and measured force versus time, with sinusoidal fit. (b) Measured force versus applied voltage, with the same fit.

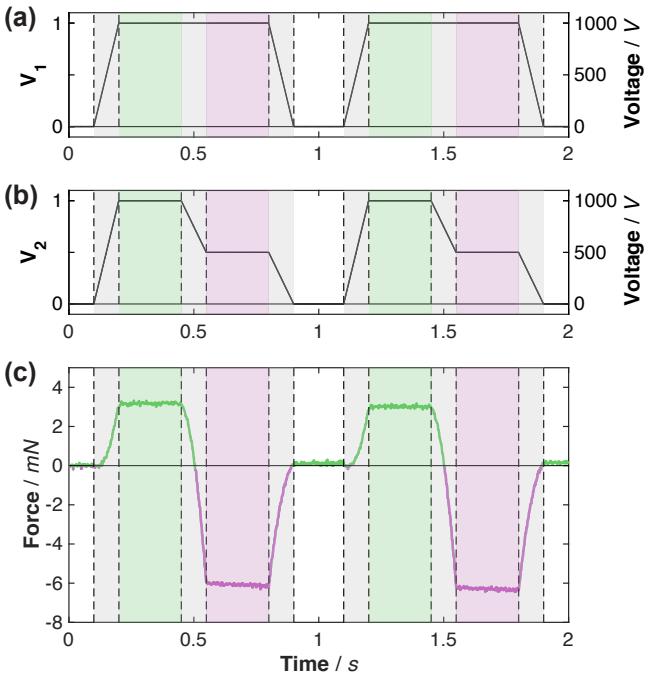

Fig. 5: RAFA with V2-A electrode pattern controllably generating repulsive- and attractive-forces at ΔZ = 100 μm and 0–1.0 kV. Commanded V_1 (a) and V_2 (b) trapezoidal signals along with measured applied voltage. (c) Measured force versus time. In (a/b), green regions represent voltage signals designed for repulsion and purple regions represent those for attraction. In (c), measured repulsive forces are green and attractive forces are purple.

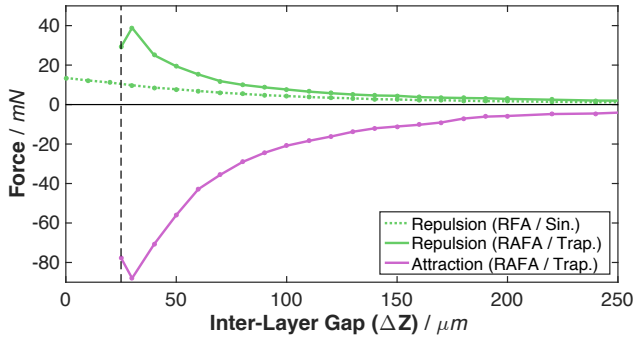

Fig. 6: Thin-film electrostatic actuator controllably generating repulsive- and attractive-forces. Measured forces for a 2.5 cm^2 actuator operating in repulsive-force (RFA) and repulsive-/attractive-force (RAFA) modes, with sinusoidal (Sin.) and trapezoidal (Trap.) waveforms. Peak applied voltage in all cases is approx. 1.2 kV. Vertical dashed line marks contact point (ΔZ = 25 μm) of the two layers (in RAFA-mode) due to an inter-layer polyimide insulator.

RFA-mode testing uses a sinusoidal signals of 0–1.2 kV and 2 Hz. RAFA-mode testing uses trapezoidal signals of 0–1.2 kV and 1 Hz (with 0.1 s ramps and 0.25 s holds at peak repulsive / attractive forces).

D. Results

Fig. 4 demonstrates the blocked-force performance of the RFA. The RFA generates smooth sinusoidal forces (the quadratic relationship between applied voltage and measured force is shown in Fig. 4b) with no discernible lag or nonlinearities. Minimal hysteresis is visible and dielectric charging results in only a 14% decrease in peak force over 10 cycles.

Fig. 5 demonstrates the blocked-force performance of the RAFA. The RAFA quickly tracks the trapezoidal waveform during voltage ramps (in grey) and maintains stable repulsive- and attractive-forces during voltage holds at 1.0 / 1.0 kV (V_1 / V_2) and 1.0 / 0.5 kV (V_1 / V_2), respectively. Note that square waveforms reduce polyimide's mean-time-to-failure [33], and are avoided. The RAFA was tested for up to 100 cycles using this waveform (at 1 Hz), with dielectric charging causing a -19% / +10% change in repulsive / attractive force after 10 cycles and -35% / +20% change after 100 cycles (amounting to a 1.2 mN decrease in peak forces). During unpowered (0 V) periods, the RAFA exhibits near-zero force production – indicating minimal residual charge.

Fig. 6 presents the actuator force versus ΔZ offset, with both sinusoidal and trapezoidal applied voltages. Peak repulsive forces of 38.9 mN (156 Pa at 2.5 cm^2 electrode area) and peak attractive forces of 80.0 mN (356 Pa) were measured at ΔZ = 30 μm and 1.2 / 0 kV (V_1 / V_2).

V. Robot Development

The Repulsive-/Attractive-Force Actuator Robot (RAFAR) is a thin-film milli-robot developed with an integrated 2-layer RAFA (Fig. 1). The assembled robot has dimensions

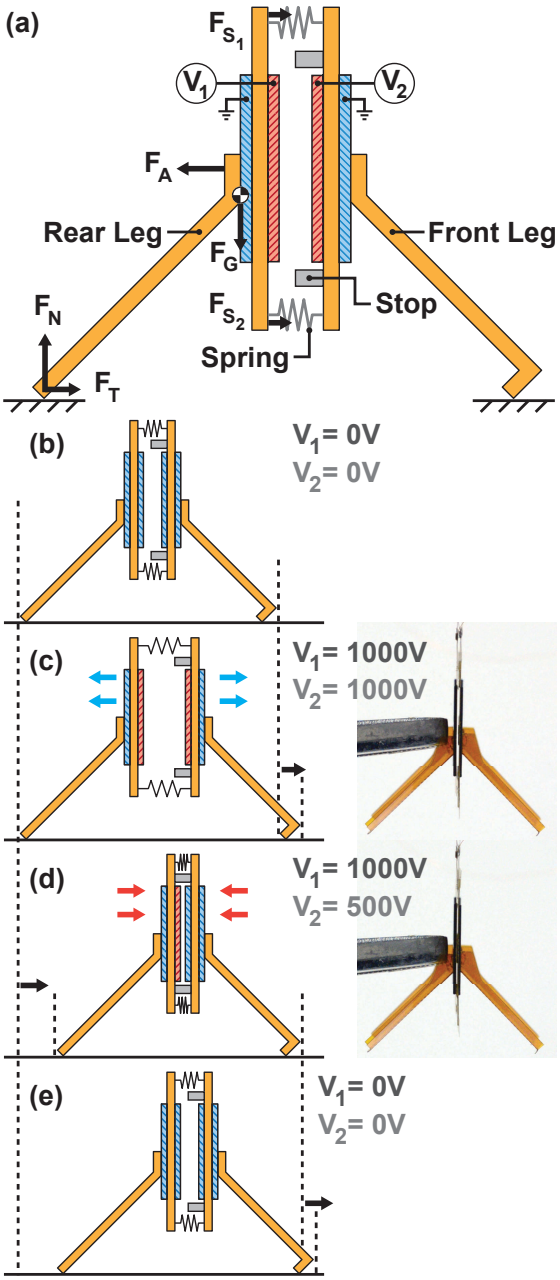

Fig. 7: RAFAR cross-section and crawling behavior – cycling between extension of the front legs (c) (with repulsive-force) and retraction of the rear legs (d) (with attractive-force).

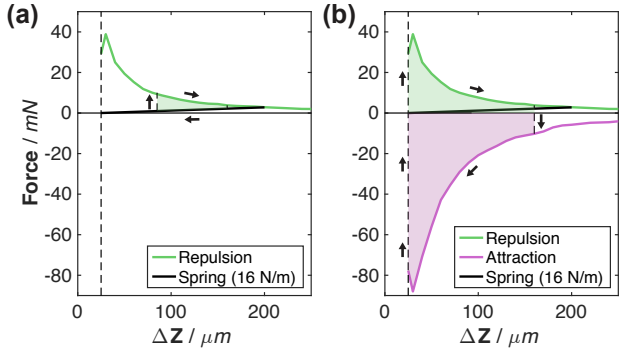

Fig. 8: Work loops for RFA (a) and RAFA (b), based on actuator (Fig 6), foot friction (Fig. 10), and spring forces. RAFAR's actuator has 42% smaller area, thus correspondingly reduced forces are expected for the fabricated robot.

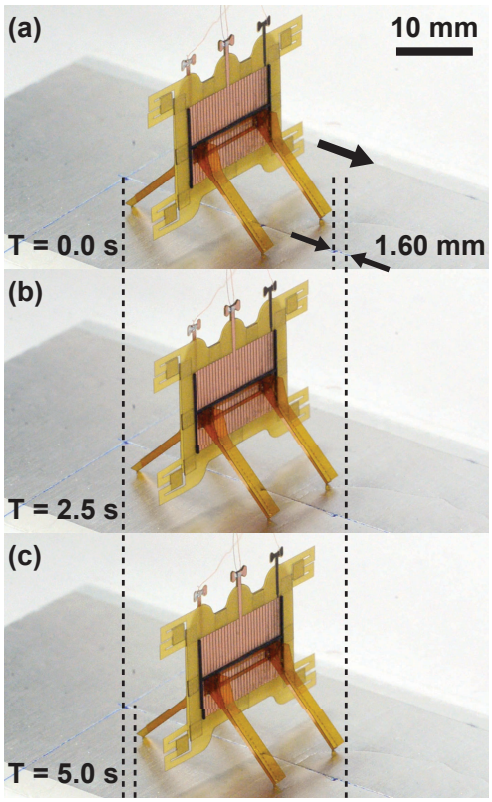

Fig. 9: RAFAR crawling sequence at the start (a), middle (b), and end (c) of 5 steps (1.60 mm traveled).

of 20 (long) x 27 (wide) x 22 (tall) mm, a total mass of 132 mg, and uses an inchworm crawling sequence to locomote (Fig. 7). The robot successfully crawls on an aluminum foil substrate at an average speed of 0.32 mm/s (0.012 BL/s) over 5 steps at 1 Hz (see **Video**), and its performance is compared to other milli-robots in Table II.

The repeating sequence of alternating repulsive-/attractive-forces used for this crawling pattern was successfully generated (Fig. 5). Use of both repulsive- and attractive-actuation substantially increases the potential work-loop (over an equivalent spring restoring force), as shown in Fig. 8. Actuator displacements require that generated actuator forces (measured in Fig. 6) be greater than measured foot friction forces (Fig. 10). This sequence also depends on foot friction anisotropy (characterized in Fig. 10) for forward motion.

A. Body Design

The RAFAR is composed of a 2-layer RAFA that was wet-etched by a commercial vendor (Sec. IV-A) and uses the V2-A electrode configuration ([300, 400, 500] μm) to ensure the highest force production possible. The RAFA layers are connected via a folded-spring suspension (4 springs located

Table II: Survey of actuators used for meso-scale walking / crawling robots. Robots with greater capabilities – untethered (Tether) and steerable (Steer) – are rated higher (+) than those without (o).

Actuator Design	**Act. / #**	**Tether**	**Steer**	**M** / *g*	**Dim.** / m^3	**Speed** / *m/s*	**BL/s** / *1/s*	**V** / *V*	**Source**
Scratch Drive Electrostatic	2	+	+	–	60 x 250 x 10 $\cdot 10^{-6}$	$2.0 \cdot 10^{-4}$	1.25	$\pm$140	[5]
Scratch Drive Electrostatic	1	o	o	–	30 x 15 x 10 $\cdot 10^{-3}$	$3.7 \cdot 10^{-4}$	0.122	4000	[6]
Zipper Electrostatic	1	o	o	0.55	60 x 10 x 10 $\cdot 10^{-3}$	$5.5 \cdot 10^{-4}$	0.009	700	[4]
Vibrating Electrostatic	1	o	o	0.047	25 x 25 x 12 $\cdot 10^{-3}$	$3.0 \cdot 10^{-2}$	1.2	2500	[3]
Vibrating Electrostatic	1	+	o	0.190	25 x 25 x 12 $\cdot 10^{-3}$	$2.0 \cdot 10^{-3}$	0.08	3000	[3]
Unimorph Piezoelectric	1	o	+	3.0	50 x 10 x 9 $\cdot 10^{-3}$	$1.4 \cdot 10^{-1}$	2.8	140	[11]
Bimorph Piezoelectric	6	o	+	1.27	44 x – x – $\cdot 10^{-3}$	$3.7 \cdot 10^{-1}$	8.4	200	[9]
Bimorph Piezoelectric	8	+	+	2.8	45 x – x – $\cdot 10^{-3}$	$1.7 \cdot 10^{-1}$	3.8	200	[10]
Shape Memory Alloy	2	+	+	2.4	30 x – x – $\cdot 10^{-3}$	$3 \cdot 10^{-2}$	1.0	13.6	[12]
RAFA	1	o	o	0.132	20 x 27 x 22 $\cdot 10^{-3}$	$3.2 \cdot 10^{-4}$	0.012	1000	This Work

Act. – Number of Actuators **M** – Mass **Dim.** – Dimensions **BL/s** – Body Lengths per Second **V** – Operating Voltage

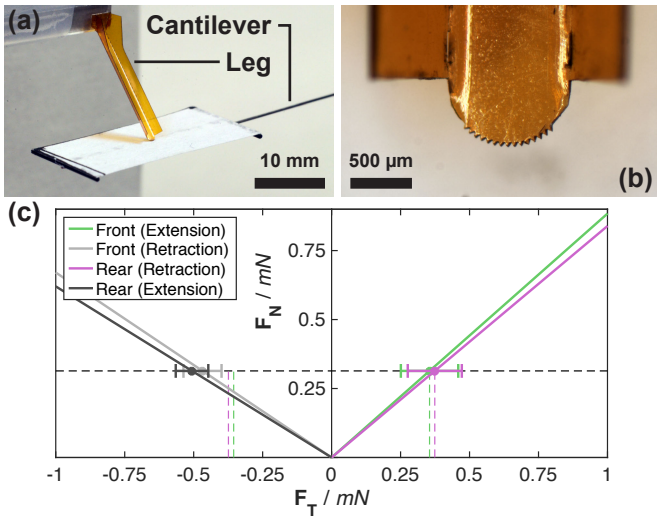

Fig. 10: Fabricated 5 mg leg on the friction-testing stand (a) with close-up of a rear foot (b). The feet exhibit anisotropic friction (c) by terminating in a circular array of 50 μm spines. The *front foot* will preferentially extend during repulsive-actuation (green) and the *rear foot* will preferentially retract during attractive-actuation (purple). Foot friction is measured with $F_N = mg/4$ (horizontal dashed line) and is lower when legs experience loading in the forward direction (vertical dashed lines, $F_T > 0$). Error bars denote 1σ (n = 6) per foot and F_T direction.

at actuator corners) that provides actuator layer alignment, mechanical constraints (compliant to normal force / stiff to shear force), and some restoring force. The RAFA is reinforced by three carbon fiber rods (Ø 280 μm) adhered to each ground electrode (to avoid affecting the electric field) and PET spacers (2 x 2 x 0.118 mm thick) that are adhered to one actuator layer around the perimeter of the internal electrodes. The spacers act as mechanical stops to maintain inter-layer spacing ($\Delta Z \geq 100$ μm) and prevent electrode contact / shorting during attractive-mode operation. Total mass is 132 mg, including: actuator (107 mg), carbon fiber reinforcement (6.0 mg), legs (19.0 mg, 4 x 4.75 mg).

Power is supplied to the robot via four 75 μm wires (V_1, V_2, and 2 V_- grounds), which are soldered directly to electrode pads on each actuator layer. The wires are routed via an overhead arm, and are lightweight and flexible to minimize impact on robot dynamics. Two high-voltage amplifiers (Trek, PZD700) power the two actuator layers.

B. Leg Design & Foot Characterization

The robot's leg design is seen in Fig. 10, mounted in a friction testing setup consisting of a paper friction pad on a cantilevered rod (k = 0.29 N/m). A known normal force (F_N) is applied to the leg and transverse force (F_T) is increased until the foot slips.

The anisotropic foot Fig. 10(b) is inspired by prior spine designs for milli-robot feet [34]–[36]. The front and rear legs are constructed of polyimide film (50 μm) with approx. 50 μm long spines. The spines contact the ground at a 45° angle pointing rearward (front legs have a 90° bend above the spines) to ensure anisotropic friction (Fig. 10c). Static friction is 1.3x greater for $F_T < 0$, ensuring feet will preferentially slide forward.

VI. Conclusion

In this paper we have demonstrated a new bidirectional, thin-film Repulsive-/Attractive-Force electrostatic Actuator (RAFA). The 2-layer RAFA employs a new, optimized electrode geometry for higher force production and is capable of controllably generating both repulsive and attractive forces by varying the applied voltage to each layer. Measured forces up to 156 Pa (38.9 mN, for 2.5 cm^2 electrode area) in repulsion and 352 Pa (88.0 mN) in attraction were generated when operating at 0–1.2 kV.

We also demonstrate the RAFAR, a 132 mg milli-robot powered by a RAFA and capable of crawling at 0.32 mm/s (0.012 BL/s) using 1 Hz / 0–1.0 kV bidirectional actuation. A future area of research is to explore a range of control signals (waveforms, voltages, and frequencies) that could provide faster crawling locomotion.

This bidirectional RAFA – capable of controllably generating repulsive- and attractive-forces – is of value to the MEMS and milli-robotics communities alike. Repulsive-force actuators provide inherently open-loop stable actuation with peak force at initial displacements. Attractive-force actuators provide a voltage-controllable restoring force with greater magnitude than a mechanical spring force. As a result, the RAFA is ideal for applications that require electrostatic actuation with greater work-loops than unidirectional actuators (with spring returns), such as the crawling robot demonstrated in this paper.

ACKNOWLEDGEMENT

We thank M. Hettick and A. Javey for use of a plasma etcher. We also thank J. Lee, C. Casarez, and J. Yim for discussions on robot body / friction forces.

Commercial fabrication of actuator layers was performed by R. Appeldorn at The Boardworks.

Funding was provided in part by the National Science Foundation's National Robotics Initiative (NRI) via grant CMMI-1427096.

REFERENCES

[1] T. Niino, S. Egawa, and T. Higuchi, "High-power and high-efficiency electrostatic actuator," in *IEEE MEMS*, pp. 236–241, 1993.

[2] H. Wang, A. Yamamoto, and T. Higuchi, "Electrostatic-motor-driven electroadhesive robot," in *IEEE/RSJ IROS*, p. 914, 2012.

[3] M. Qi, Y. Zhu, Z. Liu, X. Zhang, X. Yan, and L. Lin, "A fast-moving electrostatic crawling insect," in *MEMS*, p. 761, 2017.

[4] A. S. Chen, H. Zhu, Y. Li, L. Hu, and S. Bergbreiter, "A paper-based electrostatic zipper actuator for printable robots," in *IEEE ICRA*, p. 5038, 2014.

[5] B. Donald, C. Levey, C. McGray, I. Paprotny, and D. Rus, "An Untethered, Electrostatic, Globally Controllable MEMS Micro-Robot," *J. Microelectromech. Syst.*, vol. 15, no. 1, pp. 1–15, 2006.

[6] H. Shigemune, S. Maeda, V. Cacucciolo, Y. Iwata, E. Iwase, S. Hashimoto, and S. Sugano, "Printed paper robot driven by electrostatic actuator," *IEEE Robot. Autom. Lett.*, vol. 2, no. 2, p. 1001, 2017.

[7] K. Y. Ma, P. Chirarattananon, S. B. Fuller, and R. J. Wood, "Controlled flight of a biologically inspired, insect-scale robot.," *Science*, vol. 340, no. 6132, pp. 603–7, 2013.

[8] K. L. Hoffman and R. J. Wood, "Passive undulatory gaits enhance walking in a myriapod millirobot," in *IEEE IROS*, vol. 2, pp. 1479–1486, 2011.

[9] A. T. Baisch and R. J. Wood, "Pop-up assembly of a quadrupedal ambulatory MicroRobot," in *IEEE IROS*, pp. 1518–1524, 2013.

[10] B. Goldberg, R. Zufferey, N. Doshi, E. F. Helbling, M. Kovac, R. J. Wood, and G. Whittredge, "Power and Control Autonomy for High-Speed Locomotion With an Insect-Scale Legged Robot," *IEEE RA-L*, vol. 3, no. 2, pp. 987–993, 2018.

[11] A. G. Dharmawan, H. H. Hariri, S. Foong, G. S. Soh, and K. L. Wood, "Steerable miniature legged robot driven by a single piezoelectric bending unimorph actuator," in *IEEE ICRA*, pp. 6008–6013, 2017.

[12] A. M. Hoover, E. Steltz, and R. S. Fearing, "RoACH: An autonomous 2.4 g crawling hexapod robot," *IEEE IROS*, pp. 26–33, 2008.

[13] N. J. Kohut, A. M. Hoover, K. Y. Ma, S. S. Baek, and R. S. Fearing, "MEDIC: A legged millirobot utilizing novel obstacle traversal," in *IEEE ICRA*, p. 802, 2011.

[14] A. T. Baisch and R. J. Wood, "Design and Fabrication of the Harvard Ambulatory Micro-Robot," in *Robotics Research* (C. Pradalier, R. Siegwart, and G. Hirzinger, eds.), vol. 70, pp. 715–730, Berlin, Heidelberg: Springer, 2011.

[15] D. Vogtmann, R. St Pierre, and S. Bergbreiter, "A 25 mg magnetically actuated microrobot walking at $>$ 5 body lengths/sec," in *IEEE MEMS*, pp. 179–182, 2017.

[16] R. S. Pierre and S. Bergbreiter, "Gait Exploration of Sub-2 g Robots Using Magnetic Actuation," *IEEE RA-L*, vol. 2, no. 1, pp. 34–40, 2017.

[17] J. Qu, J. Choi, and K. Oldham, "Dynamic Structural and Contact Modeling for a Silicon Hexapod Microrobot," *Journal of Mechanisms and Robotics*, vol. 9, no. December, 2017.

[18] Z. Shen, Y. Liu, J. Zhao, X. Tang, and W. Chen, "Design and Experiment of a Small Legged Robot Operated by the Resonant Vibrations of Cantilever Beams," *IEEE Access*, vol. 5, pp. 8451–8458, 2017.

[19] E. W. Schaler, T. I. Zohdi, and R. S. Fearing, "Thin-film repulsive-force electrostatic actuators," *Sens. Actuators. A Phys.*, vol. 270, pp. 252–261, 2018.

[20] E. W. Schaler, L. Jiang, and R. S. Fearing, "Multi-Layer, Thin-Film Repulsive-Force Electrostatic Actuators for a 2-DoF Micro-Mirror," in *Actuators 2018 (to appear)*, (Bremen), p. 4, 2018.

[21] S. Bobbio, M. Kellam, B. Dudley, S. Goodwin-Johansson, S. Jones, J. Jacobson, F. Tranjan, and T. DuBois, "Integrated force arrays," in *IEEE MEMS*, p. 149, 1993.

[22] M. Ito and K. Saneyoshi, "Development of large-scale stacked-type electrostatic actuators for use as artificial muscles," *Adv. Robotics*, vol. 1864, pp. 1–9, 2014.

[23] N. Kellaris, V. Gopaluni Venkata, G. M. Smith, S. K. Mitchell, and C. Keplinger, "Peano-HASEL actuators: Muscle-mimetic, electrohydraulic transducers that linearly contract on activation," *Science Robotics*, vol. 3, no. 14, p. eaar3276, 2018.

[24] W. C. Tang, M. G. Lim, and R. T. Howe, "Electrostatic comb drive levitation and control method," *J. Microelectromech. Syst.*, vol. 1, no. 4, pp. 170–178, 1992.

[25] S. He and R. Ben Mrad, "Large-stroke microelectrostatic actuators for vertical translation of micromirrors used in adaptive optics," *IEEE Trans. Ind. Electron.*, vol. 52, no. 4, pp. 974–983, 2005.

[26] S. He and R. Ben Mrad, "Performance assessment of a multi-level repulsive-force out-of-plane microelectrostatic actuator," *Can. J. Elect. Comput. Eng.*, vol. 31, no. 2, pp. 71–75, 2006.

[27] S. He and R. Ben Mrad, "Design, modeling, and demonstration of a MEMS repulsive-force out-of-plane electrostatic micro actuator," *J. Microelectromech. Syst.*, vol. 17, no. 3, pp. 532–547, 2008.

[28] S. He, R. Ben Mrad, and J. Chong, "Repulsive-force out-of-plane large stroke translation micro electrostatic actuator," *J. Micromech. Microeng.*, vol. 21, no. 7, p. 075002, 2011.

[29] S. Towfighian, S. He, and R. Ben Mrad, "A low voltage electrostatic micro actuator for large out-of-plane displacement," in *ASME IDETC/CIE*, pp. 1–7, 2014.

[30] Keng Peng Tee, S. Ge, and F. Eng Hock Tay, "Adaptive Control of Electrostatic Microactuators With Bidirectional Drive," *IEEE Trans. Control Syst. Technol*, vol. 17, no. 2, pp. 340–352, 2009.

[31] R. Wood, E. Steltz, and R. Fearing, "Optimal energy density piezoelectric bending actuators," *Sens. Actuators. A Phys.*, vol. 119, no. 2, pp. 476–488, 2005.

[32] H. Ren, W. Wang, F. Tao, and J. Yao, "A Bi-Directional Out-of-Plane Actuator by Electrostatic Force," *Micromachines*, vol. 4, no. 4, pp. 431–443, 2013.

[33] T. Lebey, P. Castelan, G. Montanari, and I. Ghinello, "Influence of PWM-type voltage waveforms on reliability of machine insulation system," in *IEEE Int. Conf. on Harmonics and Quality of Power*, vol. 2, pp. 994–998, 1998.

[34] D. W. Haldane, C. Casarez, J. Karras, J. Lee, C. Li, A. Pullin, E. Schaler, D. Yun, A. Javey, and R. S. Fearing, "Integrated manufacture of exoskeleton and sensing for folded millirobots," *J. Mech. Robot.*, vol. 7, no. 2, p. 19, 2015.

[35] J. S. Lee and R. S. Fearing, "Anisotropic collapsible leg spines for increased millirobot traction," in *IEEE ICRA*, pp. 4547–4553, 2015.

[36] J. Lee, R. Fearing, and K.-J. Cho, "Compound Foot for Increased Millirobot Jumping Ability," in *CLAWAR*, pp. 1–8, 2016.